nature communications

Article

https://doi.org/10.1038/s41467-025-66529-7

Integrated bionic LiDAR for adaptive 4D machine vision

Received: 2 July 2025

Accepted: 7 November 2025

Published online: 23 December 2025

Check for updates

Ruixuan Chen[1,7], Yichen Wu[1,7], Ke Zhang[2,7], Chuxin Liu[3,7], Wencan Li[1,7], Yikun Chen[2], Bitao Shen[1], Zhaoxi Chen[2], Hanke Feng[2], Zhangfeng Ge[4], Yan Zhou[4], Zihan Tao[1], Xuguang Zhang[1], Weihan Xu[3], Yimeng Wang[1], Pengfei Cai[5], Dong Pan[5], Haowen Shu[1,6] ✉, Linjie Zhou[3] ✉, Cheng Wang[2] ✉ & Xingjun Wang[1,4,6] ✉

The human eye achieves high resolution and energy efficiency through adaptive focusing on pertinent details. This natural capability sets a benchmark that current machine vision systems struggle to emulate due to rigid parallel-sensing mechanisms. Efforts to achieve retinal-level resolution through brute-force scaling of channels can lead to prohibitive cost, complexity, and power consumption. Here, we address this bottleneck with a retina-inspired chip-scale LiDAR architecture featuring dynamic gazing capability. By synergizing an agile external cavity laser with reconfigurable electro-optic frequency combs, our integrated photonic platform enables coherent LiDAR with parallel, reconfigurable channels, allocating sensing resources to critical regions without global oversampling. This hardware-efficient design enables real-time comb-based 4D imaging at 0.012° beyond-retinal resolution and supports 4D-plus imaging through cooperative sensing with a camera. With its beyond-retinal resolution, dynamic gazing capability, and scalable chip-level manufacturability, this technology offers a path toward lightweight, high-performance perception across aerial, terrestrial, and marine autonomous systems.

Machine vision empowers computers and robots to interpret and analyze visual data from camera images, mimicking human visual capabilities for automation tasks[1]. Its scope has expanded beyond traditional cameras to include advanced sensors such as LiDAR, which enable precise distance measurement and 3D environmental perception[2]. High-resolution LiDARs that capture fine landscape details are essential for applications requiring accurate spatial awareness, especially in low-visibility conditions. However, unlike cameras, LiDARs require both laser emission and reception for each pixel, which limits their achievable pixel resolution. Scaling LiDAR resolution through channel duplication offers linear resolution improvement at the expense of superlinear increases in complexity and power, primarily due to duplicated hardware and calibration overhead. Moreover, globally enhancing LiDAR resolution is not resource-efficient, since not all regions in the field of view (FOV) are equally important, and may cause flooded irrelevant information to the system[3].

Nature provides invaluable insights to tackle these challenges since biological visual systems have evolved to be efficient, energy-

[1]State Key Laboratory of Photonics and Communications, School of Electronics, Peking University, Beijing, China. [2]Department of Electrical Engineering & State Key Laboratory of Terahertz and Millimeter Waves, City University of Hong Kong, Hong Kong, China. [3]State Key Laboratory of Photonics and Communications, Department of Electronic Engineering, Shanghai Jiao Tong University, Shanghai, China. [4]Peking University Yangtze Delta Institute of Optoelectronics, Nantong, China. [5]SiFotonics Technologies Co. Ltd., Beijing, China. [6]Frontiers Science Center for Nano-optoelectronics, Peking University, Beijing, China. [7]These authors contributed equally: Ruixuan Chen, Yichen Wu, Ke Zhang, Chuxin Liu, Wencan Li. ✉e-mail: haowenshu@pku.edu.cn; ljzhou@sjtu.edu.cn; cwang257@cityu.edu.hk; xjwang@pku.edu.cn

https://doi.org/10.1038/s41467-025-66529-7

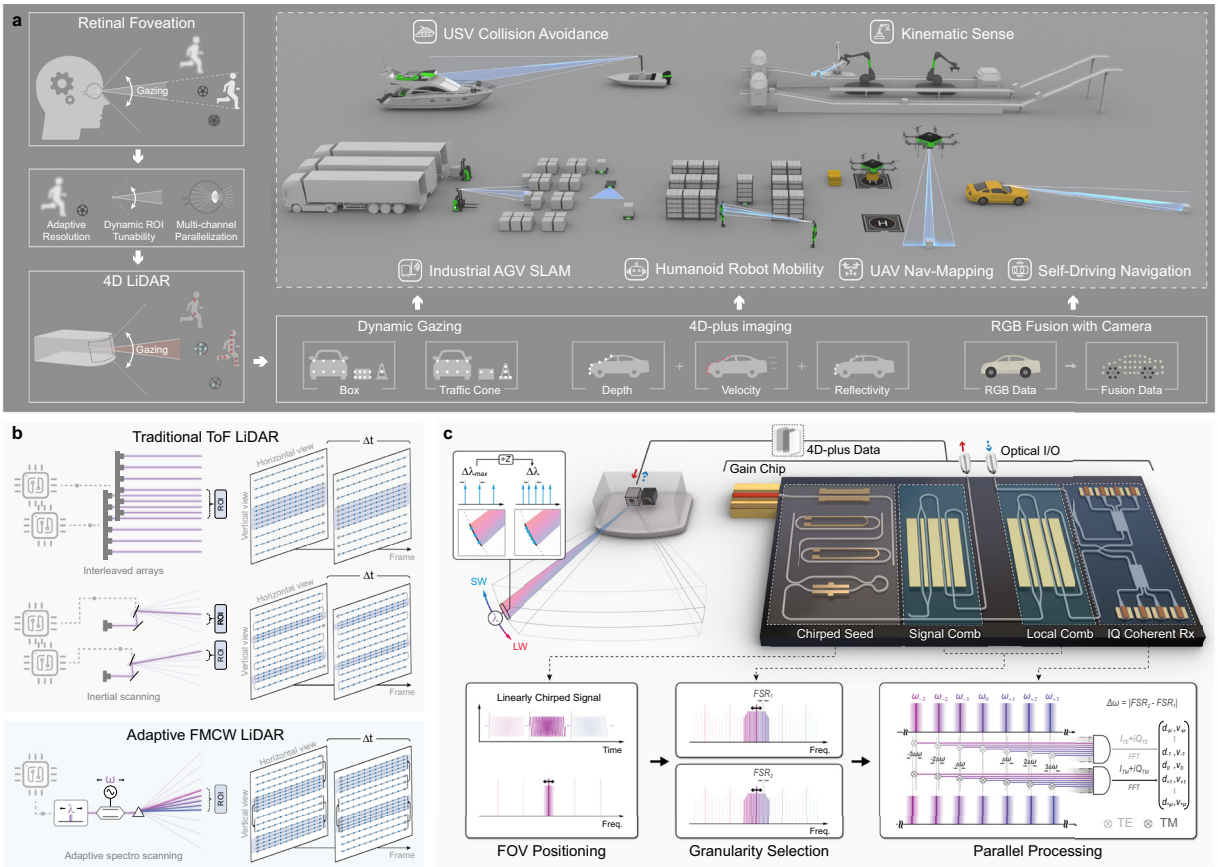

Fig. 1 | Integrated bionic LiDAR for adaptive 4D machine vision. a Top left: illustration of human retinal foveation vision, where special attention is paid to a certain ROI within a wide field of view. Bottom left: the human eye-inspired coherent 4D LiDAR, with adaptive resolution, dynamic ROI tunability, and multi-channel parallelization. Right: envisioned application scenarios of the 4D bionic LiDAR, including next-generation autonomy in Unmanned Aerial Vehicles (UAVs), Unmanned Surface Vehicles (USVs), Automated Ground Vehicles (AGVs), autonomous driving, and robotic systems. **b** Schematic comparison between traditional time-of-flight (ToF) LiDAR solutions (top) and the proposed adaptive FMCW LiDAR (bottom) for bionic vision with higher imaging resolutions in selected ROIs (dark blue regions). **c** Schematic illustration of the integrated adaptive coherent LiDAR system. Parallel chirp signals are generated by an electro-optic comb, with the spectral position controlled by the output wavelength of an on-chip tunable laser (λ). By tuning the electro-optic comb's repetition rate ($\Delta\lambda = \Delta\lambda_{max}/Z$, Z: zoom-in factor), scanning patterns with variable granularities can be projected to any desired viewpoints. All wavelength channels are received and processed by an integrated dual-polarized IQ coherent receiver to extract distance and velocity with polarization information in real time. Red arrow: multi-channel probe light; Blue arrow: received echo signal; SW short wavelength, LW long wavelength.

saving, and compact. Specifically, human eyes feature a special area in the retina, namely the macula, known for its high concentration of photoreceptors that enable precise and detailed vision[4]. Coupled with eye movements, greater attention can be paid to any region of interest (ROI) within a broad FOV (as shown in Fig. 1a top left). This provides efficient and high-quality feedback where necessary but without overwhelming the system with data from less relevant areas. Similarly, a bionic LiDAR system capable of dynamically focusing on ROIs with higher point densities could enhance perception efficiency in critical areas or search potential threats, thereby reducing hardware resource costs while approaching high-resolution imaging.

However, blending human-like perception into a compact LiDAR system design presents significant challenges, as current technologies struggle to realize adaptive resolution, dynamic ROI tunability, and multi-channel parallelization, simultaneously. Multichannel vertical-cavity surface-emitting lasers (VCSELs), for instance, can achieve high-resolution focal zones (Fig. 1b), but their static ROIs lack the dynamic adjustability required for real-time adaptive sensing[5]. Mechanical scanners, such as inertial systems, offer dynamic control over scanning area and density. However, each scanner typically only addresses one channel at a time, limiting their scalability to multi-channel scenarios, in addition to their susceptibility to mechanical fatigue[6]. Multi-wavelength light sources, such as Fourier-domain mode-locked (FDML) lasers and Kerr microcombs, provide potential pathways for parallel sensing by simultaneously projecting multiple wavelength channels toward different viewing angles. However, FDML-based parallel detection[7] only allows pre-set and immovable spectral patterns (fixed ROIs) by pre-defined time-delay configurations in the fiber loops[8], whereas Kerr frequency combs[9] with largely fixed repetition rates face challenges with adaptive imaging resolution. Moreover, none of these spectral multiplexing approaches has achieved real-time operation in dynamic environments, mainly due to the heavy hardware demands of parallel processing. In addition, the insufficient imaging resolution in current LiDAR systems pose significant barriers to their seamless integration with traditional sensors like cameras. A high-resolution LiDAR with adaptive ROIs and real-time processing capability could enable 4D-plus perception through cooperative sensing, incorporating additional information (e.g. color) from other sensors, which is essential for autonomous systems to interpret dynamic environments beyond the capabilities of human vision.

In this work, we present an integrated, retina-inspired coherent LiDAR architecture that achieves parallel, adaptive, and real-time

imaging. By synergizing an agile external-cavity laser (ECL) with reconfigurable electro-optic frequency combs, the system dynamically allocates sensing resources toward ROI without global oversampling. This hardware-efficient approach enables nuanced real-time perception that adapts to complex and dynamic environments with low latency, realizing compact 4D imaging on a chip-scale photonic platform.

Results

Concept of integrated adaptive coherent LiDAR for 4D bionic perception

Parallel and adaptive sensing is achieved by an agile ECL-pumped electro-optic comb, which generates frequency-modulated continuous laser beams across multiple wavelength channels dispersed toward distinct viewing angles (Fig. 1b bottom). This configuration enables dynamic reconfiguration of the ROI by adjusting the ECL's output wavelength and the repetition frequency of the electro-optic comb, ensuring optimal adaptability in diverse environments and applications. Unlike conventional paradigms that require bulky tunable laser arrays or optical frequency combs with massive fixed channel counts, this micro-parallelism strategy not only naturally allows adaptive imaging resolution but also reduces hardware demands by processing only a finite number of wavelength channels at a time. This effectively decouples spatial resolution from the number of parallel channels, enabling the dynamic allocation of detection channels while inherently avoiding the hardware complexity and bandwidth bottlenecks imposed by large-scale channel multiplexing. As a result, we achieve the first parallel FMCW LiDAR system with a resolution matching the human eye, enabling real-time 4D perception beyond human capability, all based on compact integrated photonic platforms.

As illustrated in Fig. 1c, our hybrid integrated chip-scale system consists of a reconfigurable parallel transmitter and an adaptive parallel receiver. The transmitter is comprised of an on-chip tunable ECL[10–14] and a signal electro-optic comb generator[15–18], both renowned for their versatile tuning capabilities. Leveraging the extensive spectral tuning range of the ECL, the viewpoints can be precisely positioned at any desired location within a broad FOV. Near the selected center wavelengths, a linear triangular frequency-modulated signal from the ECL is distributed to multiple equally spaced frequency channels using an on-chip electro-optic comb, allowing for the simultaneous illumination and detection of multiple pixels. Importantly, angular imaging resolutions at certain viewpoints can be flexibly controlled by adjusting the repetition rate of the electro-optic comb, which depends on the RF driving frequency. This adaptability enables the system to focus on any desired viewpoint within the FOV, much like the human eye's ability to gaze and focus on specific points.

On the receiver side, another electro-optic comb generator produces a local oscillator (LO) comb from the same ECL source, with a slight repetition rate offset ($\Delta\omega$ in Fig. 1c) from the signal comb. Beating between the LO comb and the received echoes down-converts the optical spectrum into a radio-frequency (RF) comb, where each comb line carries the information of a specific spatial channel. A dual-polarized in-phase (I) and quadrature (Q) coherent receiver is employed to capture both amplitude and phase of the heterodyne signals, enabling unambiguous recovery of positive and negative frequency components and thus faithful detection of all channels. The digitized RF comb signals are subsequently processed by Fourier transform with frequency-domain filtering to separate the channels, followed by peak detection for point-cloud reconstruction, thereby enabling multichannel echoes containing both static and motion information to be individually resolved through multi-heterodyne detection[19–22]. Since both comb generators share the same ECL output, common-mode laser frequency and phase noise cancel in the heterodyne beat, yielding stable intermediate frequencies. This stability alleviates the need for extensive digital drift and phase correction, thereby improving overall processing efficiency. Moreover, extracting signals from two orthogonally polarized states enhances perception by providing richer data for texture classification and robust detection. This dual polarization approach improves resistance to any signal-to-noise ratio (SNR) degradation caused by polarization changes in the return signal, ensuring consistent performance even under complicated conditions.

Adaptive parallel FMCW LiDAR source

In our adaptive parallel LiDAR scheme, the imaging FOV and granularity are controlled by the tuning range of the ECL and the repetition rate of the electro-optic comb, respectively. To achieve a wide FOV coverage, the hybrid integrated ECL is designed to include an indium-phosphide (InP) reflective semiconductor optical amplifier (RSOA) with a broad gain bandwidth, coupled with a low-loss silicon nitride (Si_3N_4) external cavity chip where the filtered feedback wavelength is widely tunable via a pair of Vernier microring resonators (MRRs), as shown in Fig. 2a. Figure 2b illustrates the superimposed spectra of laser seeds generated at ~2 nm intervals, with a wavelength tunability exceeding 100 nm and an overall side-mode suppression ratio greater than 70 dB, which serves as a chirped source for the subsequent generation of electro-optic combs at any desired wavelength.

The electro-optic comb is generated on a thin-film lithium niobate (TFLN) platform using a dual-pass phase modulator[23], which enhances modulation efficiency by doubling interaction length while maintaining a compact footprint of 11.5 mm × 0.6 mm. A slotted electrode design[24,25] is applied for better velocity matching, leading to a high electro-optic bandwidth. The excellent wavelength-reconfigurability of electro-optic combs allows us to realize efficient comb generation at a wide range of input laser wavelengths from 1510 nm to 1587 nm (as shown in Fig. 2c). The electro-optic comb is driven by a 27 dBm RF amplifier at a 43.8 GHz repetition rate. The collective spectra reveal that all generated combs across the varying wavelengths maintain uniform characteristics in terms of flatness and the number of generated lines, which is vital for ensuring consistent detection performance across a broad FOV. Importantly, point cloud scanning with different granularities (e.g. finer scan in ROIs) can be achieved by adjusting the repetition rate of the electro-optic comb without changing FOV. In our dual-pass configuration[15], the phase modulation efficiency is maximized at optimal RF frequencies that appear periodically when the recycled optical signal remains in phase with the driving microwave. Figure 2d illustrates the spectra of the electro-optic combs driven at five optimal RF frequencies from 20.4 GHz to 43.9 GHz, which are identified through electro-optic response measurements, detailed in Supplementary Section S.2. Currently, the electro-optic comb envelope generated through pure phase modulation follows the Bessel function of its first kind and is not flat. Flat-top electro-optic combs can be directly generated in the future by cascading amplitude and phase modulation (see Supplementary Section S.1), which would effectively eliminate the need for channel power shaping.

For each laser seed, linearized triangular frequency modulation is achieved by applying a pre-distorted sweep waveform to the thermal-optic phase shifters integrated into the ECL's two MRRs. This efficient modulation process enables broadband chirped signals (2.6 GHz to 4.1 GHz), modulated at a 1 kHz chirp repetition frequency (see Supplementary Section S.3). Furthermore, the frequency noise measurement results (see Supplementary Section S.4) exhibit that the intrinsic linewidths are distributed from 1 kHz to 4 kHz, while the effective 1/π-integral linewidths are around 55 kHz, which is essential for precise and long-range applications. Even faster chirp signal can be generated on the TFLN photonic platform[12,26], which is well-suited for developing high-performance frequency chirped laser.

https://doi.org/10.1038/s41467-025-66529-7

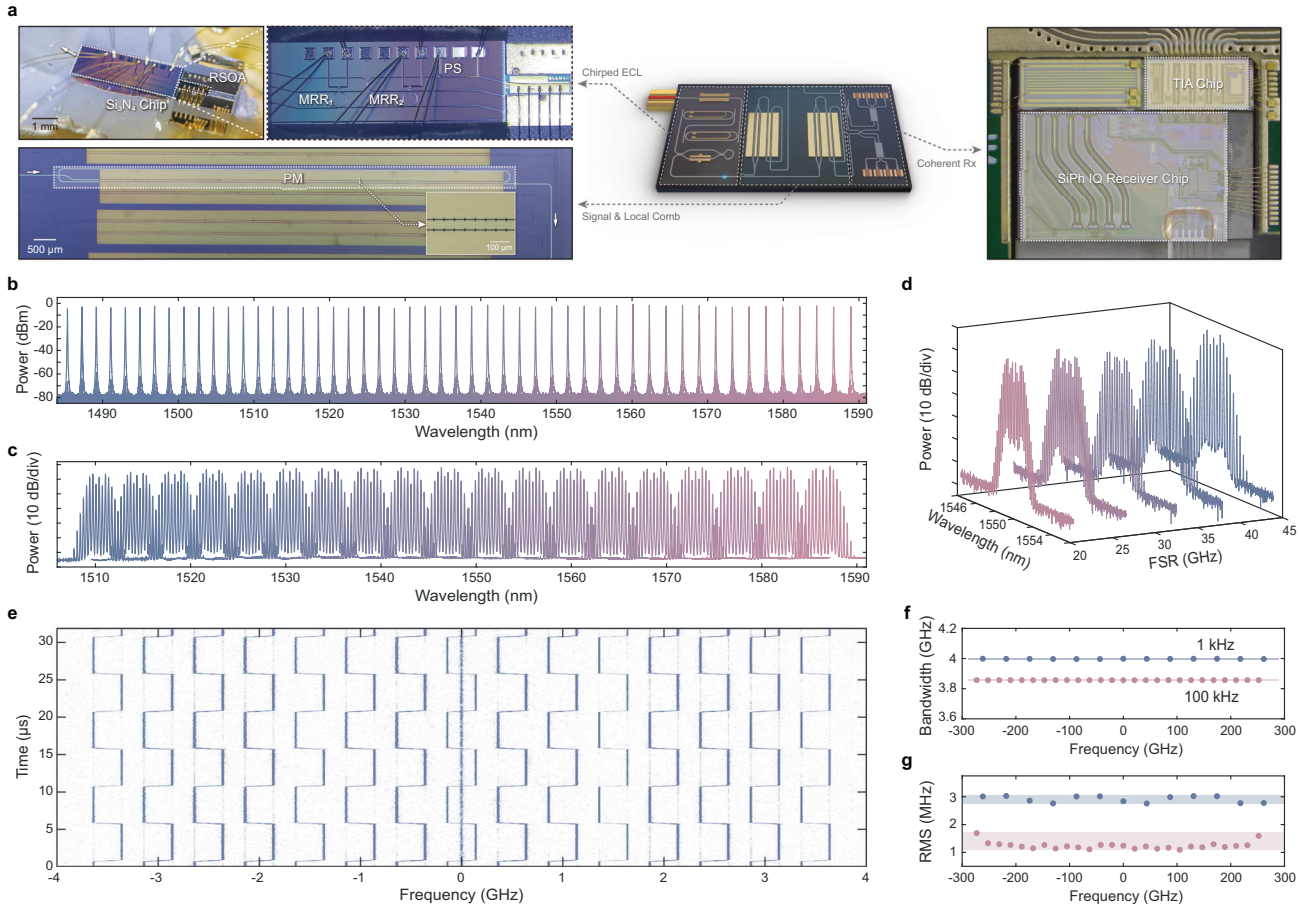

Fig. 2 | Adaptive multichannel FMCW signal generation and reception. **a** Photographs of the hybrid integrated ECL (top left), electro-optic comb generator (bottom left), and silicon photonic (SiPh) IQ receiver (right). Inset shows a zoom-in view of the slotted electrodes of the comb generator. PS, thermally tuned phase shifter; PM, phase modulator; and TIA, transimpedance amplifier. **b** Superimposed lasing spectra of the hybrid ECL, with the center wavelength of the Vernier filter scanned across the tuning range at 20 °C. **c** Broadband electro-optic combs generated at different input wavelengths from 1510 to 1587 nm. **d** Optical spectra of electro-optic combs driven by various optimal RF frequencies (20.4 GHz to 43.9 GHz) around 1550 nm. **e** Time–frequency spectrogram of multichannel heterodyne beatnotes between a signal comb (21 GHz) and local oscillator combs (20.5 GHz), measured through a 37 m delayed self-heterodyne fiber link. **f** Channel-dependent chirp bandwidth and **g** Chirp linearity from a perfect triangular frequency chirp for two electro-optic combs (21 GHz and 43.6 GHz) generated at a chirp repetition frequency of 1 kHz (blue) and 100 kHz (pink).

To demonstrate intrinsic mutual coherence between all comb lines of our parallel FMCW LiDAR source, we used 1 kHz chirped ECL to simultaneously excite two electro-optic combs (spaced at 21 GHz and 20.5 GHz) as signal comb and local oscillators. After traversing optical fibers with a length difference of 37 m, the signals were input into the SiPh coherent receiver for multi-heterodyne detection. Figure 2e shows the time-frequency map of delayed self-heterodyne beat spectroscopy. Since the frequency chirp of ECL is applied to all comb lines, they exhibit identical beat patterns. The chirp bandwidth and linearity of each channel were also experimentally verified using the heterodyne characterization setup (see Supplementary Section S.6). Unlike Kerr microcombs[19,27,28], which face degradation in chirp bandwidth due to the Raman effect and higher-order dispersion[29–31], our parallel chirp source provides superior chirp uniformity. As shown in Fig. 2f, the chirp bandwidth of the two electro-optic combs (spaced at 21 GHz and 43.6 GHz) exhibits excellent consistency, with channel-dependent chirp bandwidth deviation less than 0.054% and a maximum deviation of 2.2 MHz. Additionally, channel-dependent nonlinearity remains below 0.2%, with a maximum RMS (root mean square) below 3 MHz.

In summary, our parallel FMCW LiDAR source provides a wide spectral tuning range and flexible channel spacing, enabling both broad field coverage and fine resolution with adjustable ROIs. This allows our parallel coherent LiDAR to adaptively optimize imaging patterns to meet the varying granularity requirements in complex scenes. Furthermore, the excellent chirp consistency across channels ensures precise measurement results for each channel, enhancing detection accuracy within the global FOV.

Parallel dynamic gaze imaging beyond retina resolution

We demonstrate high-resolution gaze imaging based on our adaptive LiDAR source. A linearized triangular frequency-modulated signal with a chirp repetition frequency of 100 kHz and a 3.82 GHz chirp bandwidth is used to allow rapid detection capabilities. The signal and local oscillator combs have repetition rates differentiated by 500 MHz to ensure distinct identification of each channel during parallel processing. After optical amplification and collimation, a diffraction transmission grating is used to map the signal comb channels onto pixels in the vertical direction, while a single-axis Galvo provides the beam scanning in the horizontal direction. The received echoes and local oscillators are coupled into the coherent receiver for multi-heterodyne detection.

A 3D-printed road scene, positioned ~3.2 m in front of the Galvo mirror, includes one truck, a pedestrian, a barricade, and a box, all variably sized and placed at different spatial depths to simulate real-world conditions. With a sweep of 71 horizontal angles, our LiDAR system constructs point cloud images with resolutions of 54 × 71 pixels

https://doi.org/10.1038/s41467-025-66529-7

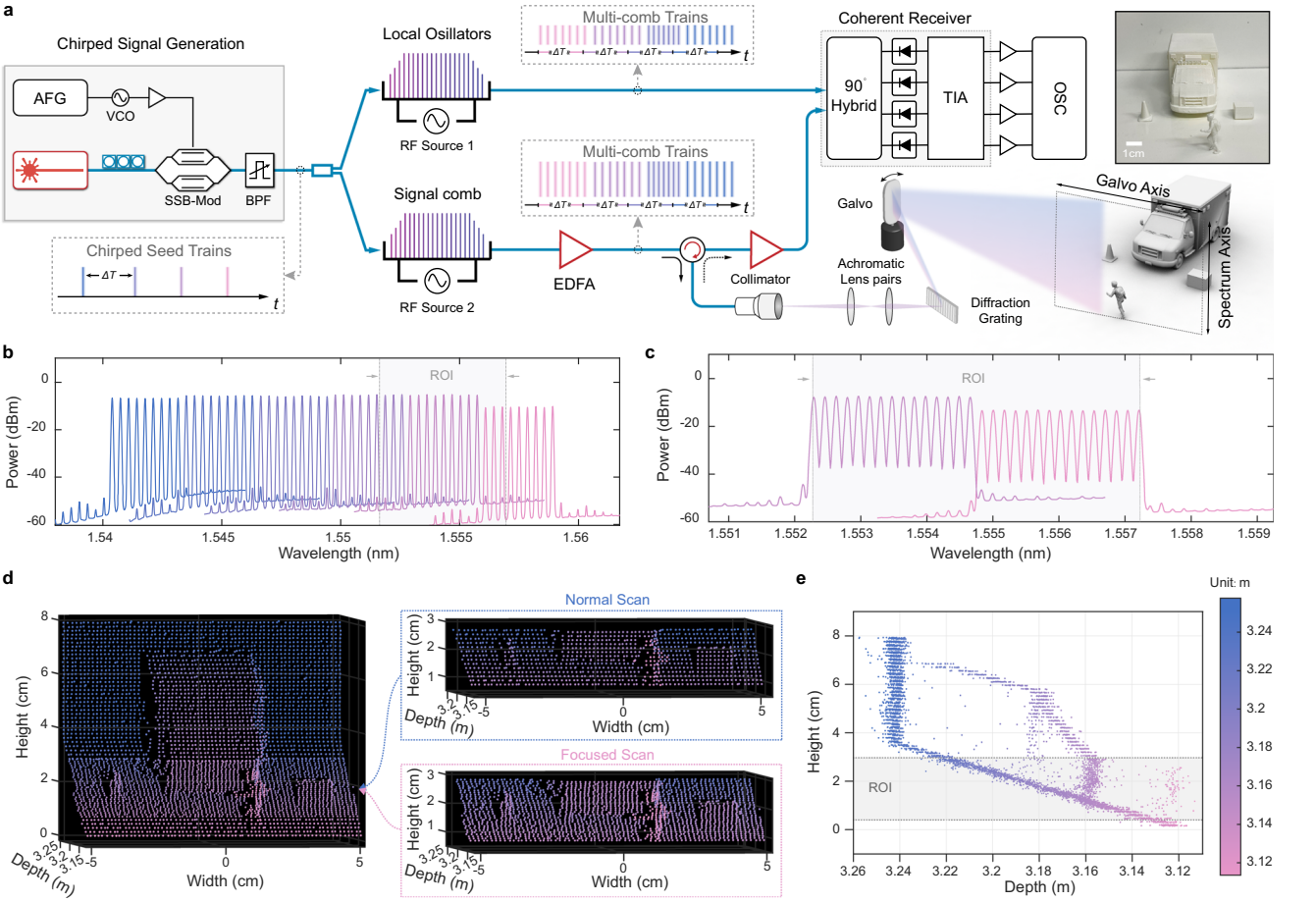

Fig. 3 | Ultra-high-resolution gaze imaging. a Experiment setup for parallel gaze imaging using two chirped electro-optic combs. Frequency modulation of the chirp seed is achieved through a single sideband modulator (SSB) driven by a voltage-controlled oscillator (VCO). Predistortion of the triangular ramp is performed with an arbitrary function generator (AFG) after linearity optimization. The valid sideband is selected by a bandpass filter (BPF). The inset photograph shows a simulated road scenario with four targets against a whiteboard background. EDFA, erbium-doped fiber amplifier; OSC, oscilloscope. **b** Optical spectra of six signal combs, with comb lines spaced at 43.5 GHz and driven by a 27 dBm RF amplifier. **c** Optical spectra of two densified electro-optic combs for gaze imaging, covering the same ROI highlighted in light gray in (**b**). **d** Reconstructed global imaging frame of the simulated road scene, with insets on the right panel showing a partially truncated global image and a gaze image centered on the small obstacle region, where the ROI is outlined by pink (focused scan) and blue (normal scan) dashed boxes. **e** Depth imaging results in a single horizontal slice of the full LiDAR imaging result shown in (**d**), with the ROI indicated by the light gray shaded area, showing significantly higher imaging resolution in the ROI.

for a standard full-FOV scan and 17 × 71 pixels for a locally dense scan centered at any vertical angle, effectively balancing broad FOV coverage and detailed imaging. Limited by the gain spectrum of the optical amplifier, 54 comb lines spaced at 43.5 GHz were used for global detection, managed by only 9 physical channels (see Fig. 3b). The resulting point cloud (as shown in Fig. 3d) clearly distinguishes background, road surface, and targets, with recognizable contours and minimal distortion.

We perform dynamic gaze imaging in a target ROI with densified scanning patterns along the spectrum axis, by re-positioning the central wavelength of the frequency chirped ECL and using electro-optic combs with smaller repetition rates. As shown in Fig. 3c, two electro-optic combs with 20.4 GHz channel spacing are utilized to focus on the regions. The focused scan, as shown in the lower inset of Fig. 3d, improves the vertical angular resolution from 0.024° in the normal scanning mode to 0.012° in the ROI. This twofold enhancement, achieved by adjusting the comb repetition rate, effectively realizes an optical zoom that reveals more intricate details beneficial for advanced tasks such as point cloud denoising and object classification. The optimal angular resolution in the ROI can achieve 0.012°, which surpasses the requirement of retina imaging (typically 1 arc minute, 0.017°). Such camera-level image capability could provide up to 15 times the resolution of conventional 3D LiDAR sensors. The precision of each point is quantified by the RMSE (root mean square error) of all valid chirp periods. Notably, 90% of the points exhibit a precision of less than 1.3 cm, with the average precision across the frame being 0.9 cm, as fitted by the Log-Normal distribution model (refer to Supplementary Section S.7). With a pixel accumulation time of 10 µs, our adaptive LiDAR allows a maximum acquisition rate of 1.7 million pixels per second. Overall, an equivalent 115-line LiDAR, calculated by dividing the FOV by the optimal angular resolution, has been demonstrated using one set of the electro-optic comb with moderate parallelism, which is comparable to current commercial LiDARs.

Adaptive colorized machine vision

Nowadays, the resolution gap between LiDAR and camera systems is posing significant challenges for achieving a seamless cooperative sensing process to map the precise 3D information of the environment. Here, leveraging the flexible gaze function with ultra-resolution, we further integrate our adaptive coherent LiDAR with a camera to achieve colorized bionic machine vision. In this demo, both the LiDAR transmitter and receiver are realized using photonic chip

https://doi.org/10.1038/s41467-025-66529-7

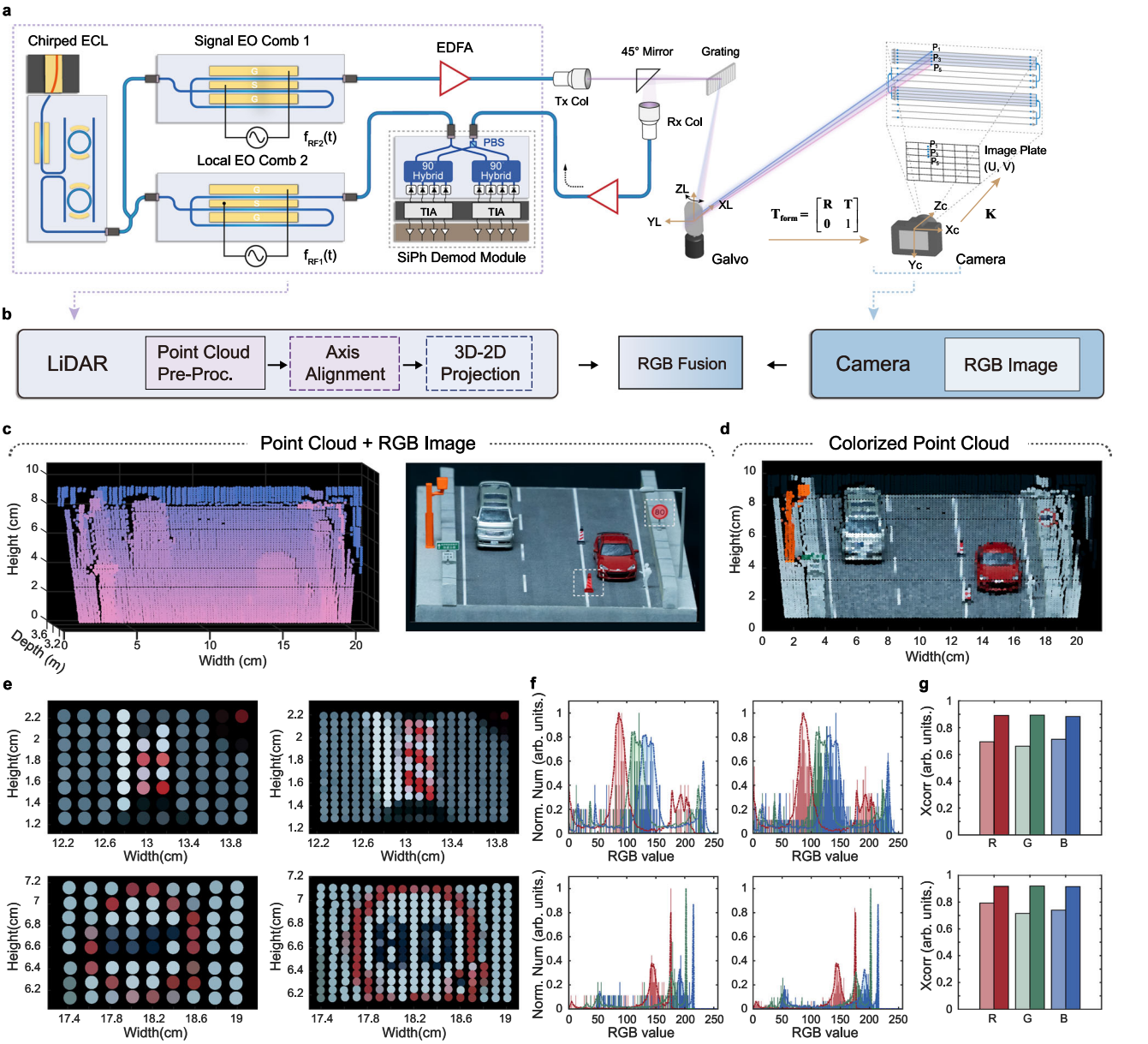

Fig. 4 | Adaptive coherent LiDAR with enhanced RGB point cloud visualization. a Experimental setup of the RGB-enhanced adaptive coherent LiDAR system, capturing synchronized point cloud data from the LiDAR and an RGB image from a high-resolution camera. PBS polarization beam splitter, COL collimator. **b** Fusion process of LiDAR and camera data. **c** Originally processed LiDAR point cloud and RGB image of a simulated road scene with a blackboard background. **d** Global colorized point cloud under a standard scan. **e** Colorized point cloud of the road sign and barricade under standard scan (left) and locally densified scan (right). **f** RGB histogram of the cropped images (envelopes marked by dashed line) and colorized point cloud in **e** (presented as bars) for the road sign (top) and barricade (bottom), respectively. **g** Cosine similarity between the image and the point cloud.

solutions as detailed in Fig. 2. As shown in Fig. 4a, multi-channel probing beams with adjustable granularity were generated using our integrated photonic LiDAR system, and stable multi-heterodyne detection was achieved via a SiPh coherent receiver in a bistatic setup (see Methods for details).

To generate colorized point clouds, our adaptive LiDAR was calibrated with the camera to ensure alignment between the captured point cloud and RGB image pixels. As illustrated in Fig. 4b, the original point cloud was converted into Cartesian coordinates, followed by joint calibration to derive the transformation matrix $\mathbf{T_{form}}$ and the camera intrinsic parameters $\mathbf{K}$, which allows us to accurately reproject the 3D point cloud onto the 2D image plane. Detailed sensor fusion processes are provided in Supplementary Section S.8.

Figure 4c shows the RGB image of the simulated road scene and the standard reconstructed point cloud with a resolution of 63 × 101 pixels under a standard full-FOV scan. Our calibrated cooperative imaging leads to a colorized point cloud depicted in Fig. 4d, which captures the background road and two cars with accurate and sufficiently detailed depth and color information. However, low-lying objects such as traffic cones may have a lower detection probability during standard scans due to inadequate point cloud coverage. This can be addressed by locally densifying the point cloud through dynamic gazing. By adjusting the chirp seed wavelength, electro-optic comb line spacing, and Galvo mirror, two areas (Fig. 4c, white dotted box) where the traffic cone and the road sign are located are assigned denser point clouds than those in the standard scan. From the comparison of the colored point cloud under the standard and

https://doi.org/10.1038/s41467-025-66529-7

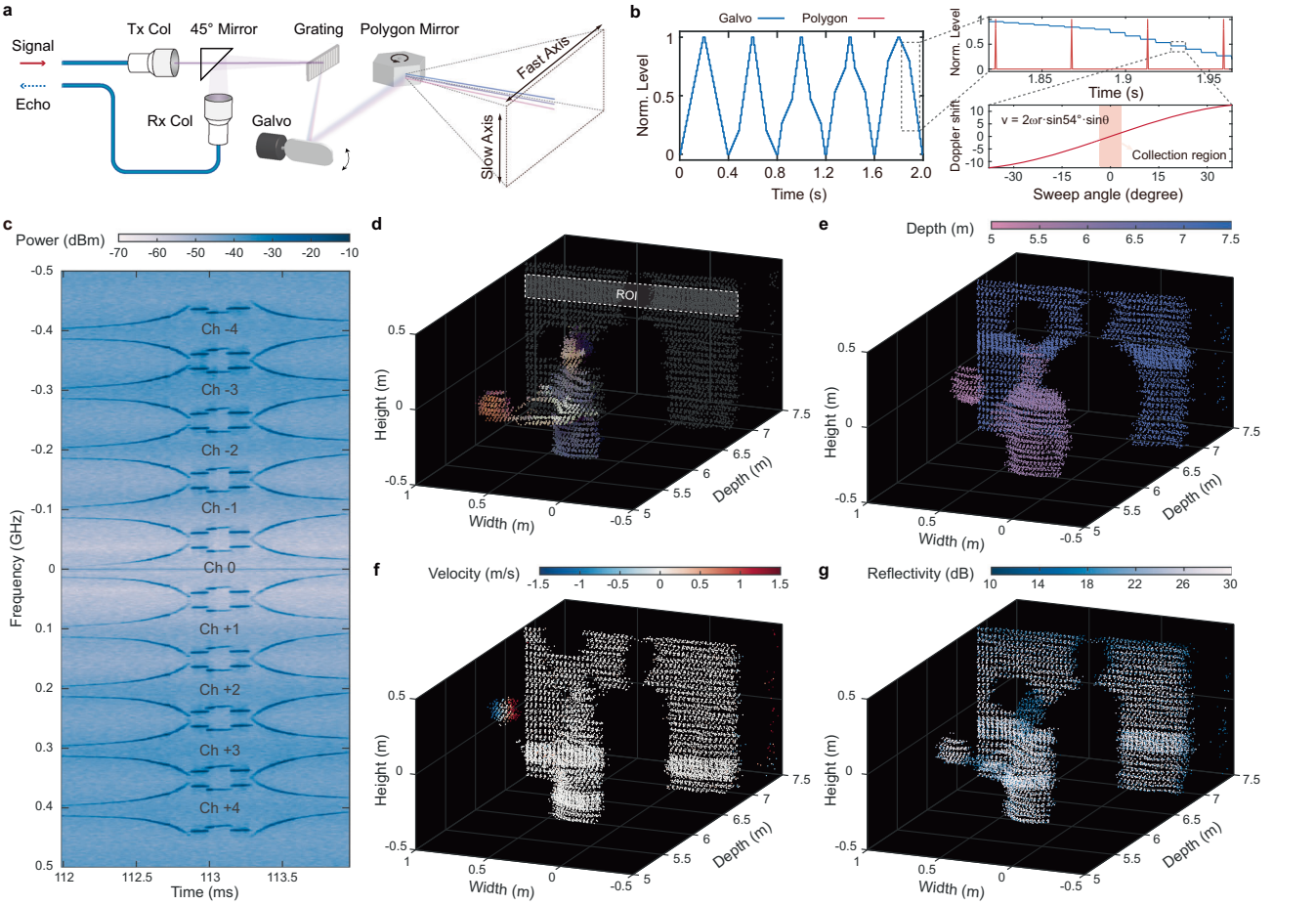

Fig. 5 | Real-time parallel 4D-plus imaging experiment. a Experiment setup of a real-time continuous spatial scanning system where a Galvo controls scanning along the slow axis and defines the position of the ROI, while a polygonal rotating mirror governs rapid fast-axis scanning. **b** Left: stepwise driving voltage of the Galvo. Top right: temporal relation between Galvo voltages (blue) and polygonal mirror pulse trains (red) corresponding to one rotation. Bottom right: the motion model of the additional Doppler shift caused by polygonal mirror rotation with sweep angles, where the red region indicates the collected horizontal FOV. **c** Time-frequency spectrogram of the complex IQ signals acquired by the SiPh coherent receiver during one full scanning cycle of the polygonal rotating mirror along the fast axis. **d** RGB-colored point cloud of the basketball tossing scenario, with white dashed lines annotating the position of the polling ROI within the current frame. The multi-dimensional detection data further incorporates **e** spatial depth, **f** velocity, and **g** reflectivity information.

focused scan (Fig. 4e), we can intuitively see the enhancement in image resolution with finer details, especially the number 80 on a road sign that was not visible in the standard scan. Moreover, Fig. 4g presents the RGB histogram comparisons between the cropped images and the colorized point cloud. The cosine similarity (see Supplementary Section S.9) between these histograms indicates an increase of approximately 10%, suggesting that the densified point cloud more closely matches the color data of the original image. The improved alignment between 3D points and image pixels provides enhanced distinction and contextual awareness of key objects, aiding in better cooperative sensing and robust decision-making. Further precision analysis of the point cloud is discussed in Supplementary Section S.10.

Real-time parallel 4D-plus imaging

To further validate the advantage of our proposed micro-parallelism architecture in achieving multidimensional sensing with reduced hardware processing demand, we demonstrate real-time parallel 4D-plus imaging under dynamic conditions. This experiment employs two chirped electro-optic frequency combs with slightly detuned line spacings (37.9 GHz and 38 GHz) to enable parallel frequency-multiplexed beam projection and multi-heterodyne detection. Benefiting from the flexibility of our light source, adaptive gazing can be realized either by tuning the comb repetition rate or by scanning the ECL wavelength alone at a fixed repetition rate, where overlapped parallel scans provide finer angular resolution. However, due to the limited tuning speed of the thermo-optic Si_3N_4 ECL, spectrum-axis scanning in our real-time demonstration was realized using a Galvo mirror for vertical control together with polygon-mirror horizontal scanning (Fig. 5a). Figure 5b illustrates the vertical stepwise driving voltage profile applied to the Galvo for fine scanning control. Although each scanning cycle covers only a subset of the field of view, the Galvo incrementally adjusts the vertical angle over time, effectively shifting the active field segment across successive frames (see magnified trace, Fig. 5b left). We further apply velocity correction based on a motion model of the rotating mirror to compensate for systematic Doppler biases (Fig. 5b right), with detailed analysis provided in Supplementary Section S.12. A time-frequency spectrogram of all comb channels during one rotation (Fig. 5c) confirms stable multi-heterodyne acquisition with sufficient SNR.

The system's real-world performance is validated in a basketball tossing scenario. The 4D-plus images were acquired with a FOV of 12.23° × 8.36° (H × V) and a fast-axis scanning rate of 250 Hz, producing a global resolution of 50 × 270 pixels (H × V). Figure 5d illustrates one real-time bionic machine vision frame through fused LiDAR-camera

data, vividly resolving the surface texture of the human face through an ROI marked by the dashed lines. To demonstrate the system's dynamic control of focused scanning segment, we deliberately shift the high-resolution region vertically across successive frames (Fig. 5e–g). While practical applications would typically hold the high-resolution region on a fixed area of interest, this stepwise sweep is used here to showcase the system's ability to reallocate resolution across the full FOV. The rotating state of the basketball can be clearly resolved from the captured velocity map, where the continuous Doppler variation over the basketball surface (Fig. 5f) reveals angular momentum, while reflectivity contrast (Fig. 5g) further enhances object classification. The theoretical ranging resolution determined by the 4 GHz chirp bandwidth is approximately 3.8 cm. Performance evaluation shows an RMSE of 1.65 cm under real-time operation, with velocity accuracy characterized by a standard deviation of 7.81 cm/s (See Supplementary Section S.13). Full-time videos of 30 seconds, showcasing the real-time 4D-plus point cloud measurements, are provided in Supplementary Video 1 and Supplementary Video 2, with a frame rate of 8 Hz, which also sets the effective refresh rate of the fused LiDAR–camera data stream. To the best of our knowledge, this represents the first demonstration of a real-time, comb-based, parallel 4D-plus LiDAR system, capable of simultaneously resolving spatial, velocity, reflectivity and color dimensions at high resolution, while maintaining hardware efficiency through micro-parallelism.

Discussion

In summary, we have demonstrated an integrated bionic LiDAR that can adaptively gaze at selected ROIs with beyond-retinal resolution, excellent scalability and tunability. These core functionalities are enabled by the efficient and coherent electro-optic interactions in TFLN platform. The generated chirp electro-optic comb source exhibits intrinsic mutual coherence between all comb lines, broadband uniformity, and convenient tunability of the repetition rate and center frequency. This results in massive equivalent scanning lines realized with a moderate number of physical channels, which is of practical significance in reducing system size and cost. Furthermore, the broadband tunability of the ECL wavelength enables solid-state positioning of the ROI anywhere within the FOV and supports continuous scanning for small obstacles. Adaptive parallel detection is facilitated through multi-heterodyne detection of two sets of electro-optic combs driven by the same chirped source.

Despite that current system demonstrates on-chip-level integration using multiple photonic components, it holds significant potential for full monolithic integration on a TFLN platform: integrated Pockels laser[14,26] can supply a rapidly chirped and spectrally scanned source; the gain and saturated output power of rare-earth-doped TFLN amplifiers[32,33] are approaching the performance of commercial fiber amplifiers. Additionally, non-mechanical beam steering is poised to be achieved through optical phased arrays[34–37] or arrays of acousto-optic devices[38]. Although the pure LN platform lacks native light sources and photodetectors, the heterogeneous integration of TFLN with other materials such as silicon[39,40], silicon nitride[41,42] or III-V compounds[43,44] can provide high-quality active devices.

With the ongoing efforts in multi-function and multi-material integration, a fully integrated artificial macular is foreseeable. Assuming full utilization of the 100 nm spectral range (1486–1590 nm) with 20.4 GHz channel spacing, an equivalent 637-line coherent LiDAR is possible, far surpassing current long-range ToF and FMCW systems while maintaining reasonable resource consumption. The ROI for scanning can also be further expanded or densified using ultra-low V_π modulators[45–47], allowing a higher modulation index to broaden the comb spectrum. Combining several compact adaptive LiDAR modules could lead to a multi-ROI machine vision system beyond traditional monocular and compound eye configurations.

With its beyond-retinal resolution, dynamic region-selective sensing, and scalable chip-integrated architecture, we envision our integrated bionic LiDAR system to provide transformative solutions in a range of emerging application scenarios. For example, the gaze-shifting ability of our LiDAR enables selective, event-driven perception aligned with neuromorphic vision strategies that prioritize attention based on motion, semantics, or learned saliency, akin to visual processing in biological systems. The reconfigurable imaging patterns could also inspire new applications in robotics. For instance, multiple adaptive LiDAR units with different channel spacings and optical parameters could be combined to form a compound-eye system, similar to the heterogeneous vision of a jumping spider. Such a configuration enables task-specific resolution and directional selectivity, making it well-suited for agile robots operating in cluttered environments. Finally, the concept of simultaneously utilizing frequency down-conversion and scalable repetition rate of electro-optic comb can be translated to other applications that require fast and fine spectral analysis[48–51], including adaptable optical communication[52], optical coherence tomography[53], compressive sensing and imaging[54], and high-resolution optical metrology[55–58].

Methods

Chirp seed generation

For frequency-chirped ECL, any section (including the RSOA, the MRRs, and the phase shifter) that changes the laser cavity round-trip phase can be modulated to generate the frequency chirp. To generate a sufficiently large chirp bandwidth, we synchronously drive the MRRs to synchronously tune the Vernier filter spectrum, while the phase shifter is applied for phase compensation. The resonance wavelengths of MRR_1 and MRR_2 remain aligned during the frequency chirp. Due to the intracavity mode competition mechanism, the lasing mode should satisfy the resonating condition of the Vernier MRR. Therefore, the lasing longitudinal mode also shifts with the Vernier filter shift. The detuning of them could be compensated via the phase shifter. In resonance, the additional phase introduced to the laser cavity by MRR_i is $\varphi_{c,i} = \frac{L_{e,i}}{L_i}\varphi_i$. L_i is the circumference of the MRR_i, while $L_{e,i}$ is the effective length of the MRR_i. The laser wavelength shift $\delta\lambda_c$ is related to the ring resonator phase change $\delta\varphi_i$ by

$$\delta\lambda_c = \sum_i \frac{FSR_{laser}}{2\pi}\frac{L_{e,i}}{L_i}\delta\varphi_i \tag{1}$$

According to the enhancement factor $L_{e,i}/L_i$, the MRR induces a wavelength shift greater than the phase shifter by applying the same phase change. The misalignment between the laser longitudinal mode and the filter passband could be compensated via the phase shifter, leading to a larger chirp bandwidth.

TFLN device fabrication

Our TFLN devices are fabricated from a commercially available x-cut LNOI wafer (4-inch, NANOLN), which includes a 500 nm LN thin film on the top, a 2 μm buried silicon dioxide layer, and a 500 μm silicon substrate. The ultraviolet (UV) and Ar^+-based reactive ion etching (RIE) systems are used to define LN optical waveguides and other structures. The entire device is then cladded with silicon dioxide by plasma-enhanced chemical vapor deposition (PECVD), while metal electrodes are fabricated using a sequence of photolithography, thermal evaporation, and lift-off processes[15]. In our design, capacitive loaded traveling wave electrodes are applied for an efficient match between microwave and optical velocity throughout the modulation region[15]. Finally, the devices are cleaved and the facets are carefully polished for end-fire fiber-to-chip coupling.

Experiment details

For the parallel imaging demo, the full FOV is scanned utilizing multiple sets of electro-optic combs with central wavelengths spaced at approximately 3 nm. Due to limitations in experimental equipment, we used two RF amplifiers with a saturation power of 27 dBm and an operating frequency from 18 GHz to 50 GHz, to generate electro-optic combs. Each set of electro-optic combs is flattened and amplified in an EDFA before emitting to the free space, and the average power of one single channel is below 10 dBm, in compliance with eye safety regulations. In experiment Parallel dynamic gaze imaging beyond retina resolution (Exp. I), a pair of 10 mm achromatic lenses is used for beam focusing to minimize spatial transmission loss. In contrast, two zoom fiber collimators are utilized to perform the same function in experiments Adaptive colorized machine vision (Exp. II) and Real-time parallel 4D-plus imaging (Exp. III). Afterward, the multi-channel chirped signals are vertically dispersed by a 966 lines/mm transmission grating before being guided to the Galvo for horizontal scanning (Exp. I and II) or dual axis scanning (Exp. III).

In Exp. I, a monostatic scheme is utilized. A fraction of the light reflected from the target retraces its original path. This light is then collected by the transmitting fiber collimator and routed to the receiver via the circulator. In Exp. II and III, the reflected light is guided to an independent optical path using a center-punched 45° mirror. This bistatic configuration improves isolation between transmit and receive paths, reducing unwanted back-reflections during coherent detection. To ensure polarization-insensitive signal recovery, a silicon photonic dual-polarization IQ coherent receiver is used to capture both orthogonal polarization components of the scattered signal. This configuration maintains stable signal-to-noise ratio across all comb channels despite polarization variations in free-space propagation.

For Multi-heterodyne detection, the reflected light of the emitted signal comb is amplified and coupled into a silicon photonic IQ coherent receiver with the reference comb. Passing through the on-chip PBS and phase-tuning devices, the signal comb and the reference comb are mixed in 90° optical hybrids and converted to photocurrent by photodetectors. After being amplified by the TIAs, the differential I and Q beat signals of both polarizations are acquired by the broadband Baluns (Marki Microwave BAL0026). In Exp. I and II, a 4-channel oscilloscope (Keysight MXR404A) with a 4 GHz operating bandwidth is employed, demonstrating minimal reliance on complex high-speed devices. For dynamic 4D-plus imaging in Exp. III, the beat signals are acquired using a 2-channel PCIe digitizer with 1 GHz bandwidth synchronized with trigger signals generated by the system-on-chip (SoC). For signal processing, the sampled I and Q signals are first re-orthogonalized using the Gram-Schmidt orthogonalization procedure (GSOP), and the complex signals I+iQ are then obtained. Then, we apply the fast Fourier transform to complex I+iQ signals, revealing the two-sided spectrum that contains information on all parallel comb lines. The collection durations for each horizontal angle are set to 625 μs, 5 ms in Exp.I and II, in order to acquire enough periods for precision analysis. In Exp. III, each horizontal scan takes 4 ms (corresponding to the 20 ms cycle of the five-faceted polygon mirror). The feasibility of the real-time processing is detailed in Supplementary Section S.15. Due to the current limitations of our FPGA programming, we perform offline processing where the acquired data are stored on a solid-state drive and later processed to reconstruct point cloud frames. To realize real-time 4D-plus imaging while maintaining accuracy and processing efficiency, the duration of a single horizontal scan is divided into partially overlapping time windows, with each horizontal angle allocated a 32.7 μs window optimized to balance signal-to-noise ratio and time resolution. After obtaining the frequency spectrum, a Gaussian peak fitting process is applied to identify the signal peak for each comb channel. Additional velocity correction is introduced to compensate for the systematic Doppler biases of rotating mirror. Once the original points are obtained, the point cloud is constructed based on the rotation mirror and Galvo angles.

LiDAR-camera calibration

To fuse the LiDAR point cloud and camera-colored pixels, we need to estimate the transformation matrix to that gives the relative rotation and translation between the two sensors. We use a custom calibration board with an 8 × 5 checkerboard pattern. Each square of the checkerboard measures precisely 13.35 mm. First, we position the calibration board in the FOV of both the LiDAR and the camera and capture a set of synchronized point-cloud data frames from the LiDAR and images from the camera. A camera (6000 × 4000 pixels) is used for the RGB image collection. Then, utilizing computer vision algorithms, we detect the checkerboard corners in the camera images and separate the point cloud corresponding to the calibration board. Therefore, we can use the detected 2D corners in the camera images and the corresponding 3D points from the LiDAR data to compute the transformation between the camera and the LiDAR coordinate systems. We adopt an algorithm from MATLAB LiDAR Toolbox that minimizes the reprojection error[59] to extract the transformation matrix. Finally, we project the overall point-cloud data onto the image and match the point cloud with image pixels, and the colored point-cloud data are acquired.

Synchronization of galvo and polygon mirror

To achieve real-time 4D-plus Imaging, we need to synchronize the Galvo (spectrum axis) and polygon mirror (horizontal axis) with high precision. The polygon mirror, featuring a five-facet reflective structure, completes five scans per rotation cycle, monitored by a photoelectric gate sensor that outputs a pulse signal at each rotation completion. The Galvo steps to the next angle after each line scan by the polygon mirror, and a full frame is captured when the Galvo reaches its final angle and the polygon mirror completes the last line scan. The SoC processes the polygon mirror's pulse signals to calculate its angular velocity and position in real time, generating driving signals for the Galvo and trigger signals for data acquisition. This synchronization ensures continuous, real-time point cloud data capture and high-resolution 4D-plus frame generation. Additionally, real-time monitoring of the polygon mirror's speed and position, combined with feedback control, dynamically adjusts the driving signals to counteract mechanical vibrations or speed fluctuations, maintaining scanning accuracy and data consistency.

Data availability

The data that supports the plots within this paper and other findings of this study are available on Zenodo (https://doi.org/10.5281/zenodo.17414670). Additional data are available from the corresponding author upon request.

Code availability

The codes that support the findings of this study are available from the corresponding authors upon reasonable request.

References

1. Davies, E. R. et al. Computer and machine vision: theory, algorithms, practicalities. (Academic Press, 2012).
2. Yeong, D. J. et al. Sensor and sensor fusion technology in autonomous vehicles: a review. *Sensors* **21**, 2140 (2021).
3. https://www.aeye.ai/resources/whitepapers/rethinking-the-four-rs-of-lidar-rate-resolutionreturns-range-2/. AEye (white paper).
4. Hussey, K. A. et al. Patterning and development of photoreceptors in the human retina. *Front. Cell Dev. Biol.* **10**, 878350 (2022).

5. Liang, D. et al. Evolution of laser technology for automotive LiDAR, an industrial viewpoint. *Nat. Commun.* **15**, 7660 (2024).
6. Wang, D. et al. MEMS mirrors for LiDAR: a review. *Micromachines* **11**, 456 (2020).
7. Zang, Z. et al. Ultrafast parallel single-pixel LiDAR with all-optical spectro-temporal encoding. *APL Photonics* **7**, 046102 (2022).
8. Yegnanarayanan, S. et al. Recirculating photonic filter: a wavelength-selective time delay for phased-array antennas and wavelength code-division multiple access. *Opt. Lett.* **21**, 740–742 (1996).
9. Anderson, M. H. et al. Zero dispersion Kerr solitons in optical microresonators. *Nat. Commun.* **13**, 4764 (2022).
10. Liu, C. et al. Highly-linear and wavelength-tunable frequency-modulated continuous-wave hybrid integrated laser. *Laser Photonics Rev.* **18**, 2300882 (2024).
11. Lukashchuk, A. et al. Photonic-electronic integrated circuit-based coherent LiDAR engine. *Nat. Commun.* **15**, 3134 (2024).
12. Wang, S. et al. High-Performance Integrated Laser Based on Thin-Film Lithium Niobate Photonics for Coherent Ranging. *Laser Photonics Rev.* **18**, 2400224 (2024).
13. Lihachev, G. et al. Frequency agile photonic integrated external cavity laser. *APL Photonics* **9**, 126102 (2024).
14. Franken, C. A. A. et al. High-power and narrowlinewidth laser on thin-film lithium niobate enabled by photonic wire bonding. *APL Photonics* **10**, 026107 (2025).
15. Zhang, K. et al. A power-efficient integrated lithium niobate electro-optic comb generator. *Commun. Phys.* **6**, 17 (2023).
16. Zhang, M. et al. Broadband electro-optic frequency comb generation in a lithium niobate microring resonator. *Nature* **568**, 373–377 (2019).
17. Hu, Y. et al. High-efficiency and broadband on-chip electro-optic frequency comb generators. *Nat. Photonics* **16**, 679–685 (2022).
18. Rueda, A. et al. Resonant electro-optic frequency comb. *Nature* **568**, 378–381 (2019).
19. Lukashchuk, A. et al. Dual chirped microcomb based parallel ranging at megapixel-line rates. *Nat. Commun.* **13**, 3280 (2022).
20. Wang, Q. et al. Dual-comb photothermal spectroscopy. *Nat. Commun.* **13**, 2181 (2022).
21. Burghoff, D. et al. Computational multiheterodyne spectroscopy. *Sci. Adv.* **2**, e1601227 (2016).
22. Chomet, B. et al. Heterodyne coherent detection of the electric field temporal trace emitted by frequency modulated comb lasers. *Optica* **11**, 1220–1225 (2024).
23. Yu, M. et al. Integrated femtosecond pulse generator on thin-film lithium niobate. *Nature* **612**, 252–258 (2022).
24. Kharel, P. et al. Breaking voltage–bandwidth limits in integrated lithium niobate modulators using microstructured electrodes. *Optica* **8**, 357–363 (2021).
25. Xu, C. et al. 6.48 Tb/s Transmissions Using 50 GHz Integrated Lithium Niobate Flat-Top Electro-Optic Combs. *2024 Optical Fiber Communications Conference and Exhibition (OFC)*, 1–3 (IEEE, 2024).
26. Li, M. et al. Integrated Pockels laser. *Nat. Commun.* **13**, 5344 (2022).
27. Riemensberger, J. et al. Massively parallel coherent laser ranging using a soliton microcomb. *Nature* **581**, 164–170 (2020).
28. Shu, H. et al. Submilliwatt, widely tunable coherent microcomb generation with feedback-free operation. *Adv. Photonics* **5**, 036007–036007 (2023).
29. Karpov, M. et al. Raman self-frequency shift of dissipative Kerr solitons in an optical microresonator. *Phys. Rev. Lett.* **116**, 103902 (2016).
30. Cherenkov, A. V. et al. Dissipative Kerr solitons and Cherenkov radiation in optical microresonators with third-order dispersion. *Phys. Rev. A* **95**, 033810 (2017).
31. Yi, X. et al. Single-mode dispersive waves and soliton microcomb dynamics. *Nat. Commun.* **8**, 14869 (2017).
32. Liu, Y. et al. A photonic integrated circuit–based erbiumdoped amplifier. *Science* **376**, 1309–1313 (2022).
33. Wang, Y. et al. Erbium-doped lithium niobate on insulator waveguide amplifier with ultra-high internal net gain of 38 dB. *CLEO Appl. Technol.* ATu4M–3 (2024).
34. Sun, J. et al. Large-scale nanophotonic phased array. *Nature* **493**, 195–199 (2013).
35. Liu, Y. et al. Silicon optical phased array with a 180-degree field of view for 2D optical beam steering. *Optica* **9**, 903–907 (2022).
36. Chen, B. et al. SiN-On-SOI optical phased array LiDAR for ultra-wide field of view and 4D sensing. *Laser Photonics Rev.* **18**, 2301360 (2024).
37. Xu, W. et al. Aliasing-free optical phased array beamsteering with a plateau envelope. *Opt. Express* **27**, 3354–3368 (2019).
38. Li, B. et al. Frequency–angular resolving LiDAR using chip-scale acousto-optic beam steering. *Nature* **620**, 316–322 (2023).
39. He, M. et al. High-performance hybrid silicon and lithium niobate Mach–Zehnder modulators for 100 Gbit s^{-1} and beyond. *Nat. Photonics* **13**, 359–364 (2019).
40. Xiang, C. et al. High-performance lasers for fully integrated silicon nitride photonics. *Nat. Commun.* **12**, 6650 (2021).
41. Churaev, M. et al. A heterogeneously integrated lithium niobate-on-silicon nitride photonic platform. *Nat. Commun.* **14**, 3499 (2023).
42. Snigirev, V. et al. Ultrafast tunable lasers using lithium niobate integrated photonics. *Nature* **615**, 411–417 (2023).
43. Guo, X. et al. High-performance modified uni-traveling carrier photodiode integrated on a thin-film lithium niobate platform. *Photonics Res.* **10**, 1338–1343 (2022).
44. Zhang, X. et al. Heterogeneous integration of III–V semiconductor lasers on thin-film lithium niobite platform by wafer bonding. *Appl. Phys. Lett.* **122**, 081103 (2023).
45. Liu, X. et al. Broadband meandered thin-film lithium niobate modulator with ultra-low half-wave voltage. *IEEE Photonics Technol. Lett.* **34**, 424–427 (2022).
46. Li, H. et al. Compact thin-film lithium niobate modulators using slotted coplanar waveguide electrode suitable for high-volume fabrication. *J. Phys. D: Appl. Phys.* **56**, 154001 (2023).
47. He, Y. et al. Chip-scale high-performance photonic microwave oscillator. *Sci. Adv.* **10**, eado9570 (2024).
48. Shams-Ansari, A. et al. Thin-film lithium-niobate electro-optic platform for spectrally tailored dual-comb spectroscopy. *Commun. Phys.* **5**, 88 (2022).
49. Qing, T. et al. Vector spectrometer with Hertz-level resolution and super-recognition capability. *arXiv preprint* arXiv:2402.09752 (2024).
50. Xu, B. et al. Broadband and high-resolution electro-optic dual-comb interferometer with frequency agility. *Opt. Express* **27**, 9266–9275 (2019).
51. Wang, S. et al. Fast MHz spectral-resolution dual-comb spectroscopy with electro-optic modulators. *Opt. Lett.* **44**, 65–68 (2018).
52. Lukens, J. M. et al. All-optical frequency processor for networking applications. *J. Lightwave Technol.* **38**, 1678–1687 (2019).
53. Siddiqui, M. et al. High-speed optical coherence tomography by circular interferometric ranging. *Nat. Photonics* **12**, 111–116 (2018).
54. Giorgetta, F. et al. Free-form dual-comb spectroscopy for compressive sensing and imaging. *Nat. Photonics* **9**, 1312–1319 (2024).
55. Udem, T. et al. Optical frequency metrology. *Nature* **416**, 233–237 (2002).
56. Weimann, C. et al. Silicon photonic integrated circuit for fast and precise dual-comb distance metrology. *Opt. Express* **25**, 30091–30104 (2017).

57. Weimann, C. et al. Fast high-precision distance metrology using a pair of modulator-generated dual-color frequency combs. *Opt. Express* **26**, 34305–34335 (2018).
58. Tran, D. B. A. et al. Near-to mid-IR spectral purity transfer with a tunable frequency comb: Methanol frequency metrology over a 1.4 GHz span. *APL Photonics* **9**, 030801 (2024).
59. Zhou, L. et al. Automatic extrinsic calibration of a camera and a 3D lidar using line and plane correspondences. *2018 IEEE/RSJ International Conference on Intelligent Robots and Systems (IROS)*, 5562–5569 (2018).

Acknowledgements

This work was supported by National Key R&D Program of China (Grant No.2022YFB2802400), National Natural Science Foundation of China under Grant (62235002, 62327811, 62322501, 12204021, 1230040593), China National Postdoctoral Program for Innovative Talents (BX20240014), Research Grants Council, University Grants Committee (CityU 11212721, C1002-22Y, STG3/E-704/23-N), Croucher Foundation (9509005) and High performance Computing Platform of Peking University. We thank Weiji He and Chen Wang for fruitful discussions. We thank C. F. Yeung, S. Y. Lao, C. W. Lai, and L. Ho at the Nanosystem Fabrication Facility at the Hong Kong University of Science and Technology for technical support with the stepper lithography and plasma-enhanced chemical vapour deposition process. We thank W. H. Wong and K. Shum at CityU for their help in device fabrication and measurement. The CityU nano-fabrication facility was used.

Author contributions

The experiments were conceived by R.C., Y.Wu, and C.L. The devices were designed by K.Z., Y.C., and C.L. The TFLN devices were fabricated by Z.C., H.F. LiDAR-camera calibration was conducted by W.L., Z.G., and Y.Z. contributed to the packaging of the device. P.C. and D.P. provided the silicon photonic coherent receiver used in the experiments. Other characterizations were conducted by R.C., Y.Wu, and C.L., with the assistance of Y.C., W.L., B.S., Z.T., X.Z., and Y.Wang. R.C., Y.Wu, W.L., and K.Z. analyzed the results. All authors participated in writing the manuscript. The project was coordinated by K.Z. and W.X. under the supervision of H.S., L.Z., C.W., and X.W.

Competing interests

K.Z., Z.C., H.F., and W.C. are involved in developing lithium niobate technologies at RhinoptiX Limited. The remaining authors declare no competing interests.

Additional information

Supplementary information The online version contains supplementary material available at https://doi.org/10.1038/s41467-025-66529-7.

Correspondence and requests for materials should be addressed to Haowen Shu, Linjie Zhou, Cheng Wang or Xingjun Wang.

Peer review information *Nature Communications* thanks the anonymous reviewer(s) for their contribution to the peer review of this work. A peer review file is available.